Blume-Capel Ising ferromagnet with competing crystal-field interactions

Daniel P. Snowman

Department of Physical Sciences, Rhode Island College, Providence, Rhode Island 02908, USA
(Received 25 November 2008; published 17 April 2009)

This investigation employs a hierarchical lattice and renormalization-group methodology to probe the effects of competing crystal-field interactions in a Blume-Capel Ising system. Several phase diagrams have been produced in temperature–crystal-field space as the strength of the competing crosslink crystal-field interactions is varied. Each sink has been interpreted and critical exponents have been calculated for the higher-order transitions.

I. INTRODUCTION

The Blume-Capel model [1,2] is a spin-1 Ising model with a Hamiltonian having bilinear (J_{ij}) and crystal-field (Δ_{ij}) interactions.

$$-\beta H = \sum_{\langle ij \rangle} J_{ij} s_i s_j - \sum_{\langle ij \rangle} \Delta_{ij}(s_i^2 + s_j^2) \quad \text{with} \ s_i = 0, \pm 1.$$
(1)

In addition to the typical Ising spin states ($s_i \pm 1$), this model allows for the presence of nonmagnetic impurities with $s_i = 0$. Magnetic ordering is directly effected by the bilinear interactions, whereas the concentration of nonmagnetic impurities, or annealed vacancies, is directly related to the crystal-field interaction ($\sim \Delta/J$). Systems driven by fluctuations in both magnetization and density are particularly well suited for study using this model. Each term in the Hamiltonian in Eq. (1) involves summations over nearest-neighbor $\langle ij \rangle$ pairs of our lattice unit structure including the crystal-field interaction term. The reader should note that, traditionally, the summation for the crystal-field contribution is over the sites of the lattice; the current investigation has shifted this summation to the bonds, for computational convenience, with no loss of generality.

Ising systems, with density as an added degree of freedom, have been used to effectively study a wide range of systems: the superfluid transition in He^3-He^4 mixtures [3], materials with mobile defects, structural glasses [4], binary fluids, binary alloys, frustrated percolation [5], and frustrated Ising lattice gas systems [6,7]. The Blume-Capel model, in particular, has been used recently as a simple spin model for probing the phenomenon of inverse melting. The reader is directed to Schupper and Shnerb [8], and references therein, for a survey of some experimental realizations (e.g., polymers, micelles, colloids, etc.) exhibiting inverse melting or freezing.

The effects upon criticality and resulting phase diagrams, due to underlying competing interactions in various Blume-Emery-Griffiths (BEG) systems—these BEG systems also having biquadratic exchange interactions—can become very complex. Many novel types of competing interactions have been the focus of previous studies using the Blume-Emery-Griffiths model in conjunction with mean-field methods [9–12] and/or renormalization-group (RG) techniques [13–19].

Renormalization-group methods have been employed to probe the effects of competing bilinear interactions [14] in a spin-1/2 Ising model, annealed vacancies in a spin glass [18], competing biquadratic interactions in a dilute Ising ferromagnet [19], and competing crystal-field and biquadratic interactions in a BEG ferromagnet [17]. Each of these studies was conducted using a hierarchical lattice with tuning parameters allowing for the degree of frustration to be varied.

In other studies, the effects of quenched random bonds [20] and quenched random fields [21] upon the criticality and phase diagrams in BEG systems have been the primary focus. Branco *et al.* considered the effects of random crystal fields using real-space RG [15,16] and mean-field approximations [15,22] for both Blume-Capel and Blume-Emery-Griffiths model Hamiltonians, respectively.

The present investigation complements these earlier works as it employs a hierarchical lattice and renormalization-group methodology to probe the effects of competing crystal-field interactions in a Blume-Capel Ising system. In particular, system temperature ($\sim 1/J$), concentration of nonmagnetic impurities ($\sim \Delta/J$), and strength of competing crosslink crystal-field interactions are varied and phase diagrams produced. In each, the phase sinks are interpreted and critical exponents are calculated for the higher-order transitions.

II. HIERARCHICAL LATTICES AND RENORMALIZATION-GROUP THEORY

Hierarchical lattices have been effectively employed to study random-bond [23], random-field [24], spin-glass [18,25], frustrated [14,17,19], directed-path [26], and dynamic scaling [27] systems. The basic algorithm for generating a hierarchical lattice consists of two steps: defining a basic generating unit consisting of spin sites and interactions and repeatedly replacing each bond of the generating unit with the generating unit itself. The result is a self-similar infinite lattice. Figure 1 illustrates the construction of a generic hierarchical lattice. Figure 2 illustrates the construction of a slightly more complex hierarchical lattice using a basic generating unit with competing crosslink interactions [28,29].

These types of lattices are attractive to use as model systems since exact renormalization-group recursion relations can be calculated. Exact relationships connecting the coupling coefficients at two different length scales allow us to
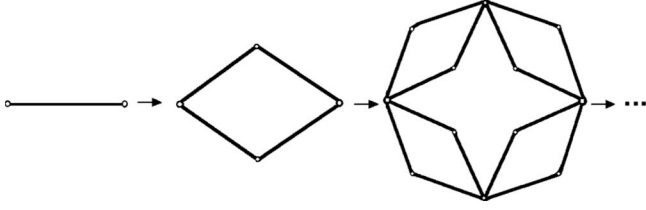
FIG. 1. Hierarchical lattices are generated by repeatedly replacing each bond with the basic unit itself [28].

calculate phase diagrams and critical exponents very accurately. Consequently, the results presented here may be considered exact on the infinite self-similar fractal lattice used, or the results may stand as approximations into the impact of competing crystal-field interactions on more realistic lattices.

In hierarchical models, such as those shown in Figs. 1 and 2, a renormalization-group solution removes internal degrees of freedom as the length scale is changed. Essentially, renormalization corresponds to the construction process, in reverse (as shown in Fig. 1). The internal degrees of freedom eliminated with each renormalization in the current study are represented by solid black dots in Figs. 2(a) and 2(b), and, represented by s_i and s_j in Eq. (5).

Demanding the partition function be preserved at each length scale allows for the derivation of the recursion relations relating the coupling coefficients at the two length scales. The effective interactions J' and Δ' are separated by a distance l' which is b lattice constants in the original system, where b is the length rescaling factor of the renormalization-group transformation. Renormalization may lead to nonzero biquadratic (K) interactions. Therefore, we write

$$\zeta_{l'}(J',K',\Delta') = \zeta_l(J,K,\Delta) \qquad (2)$$

$$\text{with } l' = bl, \qquad (3)$$
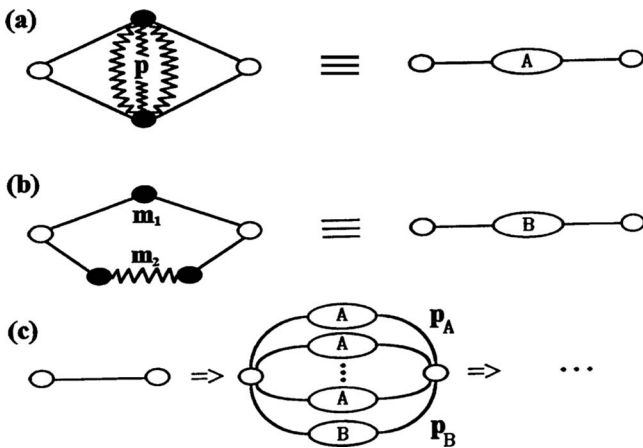
FIG. 2. The specific hierarchical lattice used in this study has two type of nearest-neighbor site interactions. Those with (J,Δ) couplings (solid lines) and those with $(J,-\Delta)$ couplings (jagged lines) (reprinted from [17] with permission from Elsevier).

TABLE I. Phases and corresponding sinks.

Phase	Sink	Characteristics
Paramagnetic I	$J \rightarrow 0$	Dense sublattice I
	$\Delta \rightarrow -\infty$	Dilute sublattice II
Ferromagnetic I	$J \rightarrow +\infty$	Dense sublattice I
	$\Delta \rightarrow -\infty$	Dilute sublattice II
Paramagnetic II	$J \rightarrow 0$	Dense sublattice II
	$\Delta \rightarrow +\infty$	Dilute sublattice I
Ferromagnetic II	$J \rightarrow +\infty$	Dense sublattice II
	$\Delta \rightarrow +\infty$	Dilute sublattice I

$$\zeta_l = \sum_s \exp[-\beta H] = \sum R_l(s_i, s_j) \qquad (4)$$

$$\text{with } R_l(s_i, s_j) = \sum_{\langle ij \rangle} \exp[-\beta H], \qquad (5)$$

$$\zeta_{l'} = \sum_{s'} \exp[-\beta H'] = \sum R_l(s_i', s_j') \qquad (6)$$

$$\text{with } R_l(s_i', s_j') = \sum_{\langle ij \rangle} \exp[J's_is_j + K's_i^2s_j^2 - \Delta'(s_i^2 + s_j^2) + \widetilde{G}'], \qquad (7)$$

where $\widetilde{G}'$ is a constant used to calculate the free energy.

The penultimate intermediate step in deriving the actual renormalization-group relationships involves equating those contributions $[R_l(s_i, s_j)$ and $R_{l'}(s_i, s_j)]$ to each partition function ($\zeta_{l'}$ and ζ_l). Note, these contributions correspond to the same configuration of end spins (s_i, s_j). These contributions, at the two different length scales, l and l', are shown in Eqs. (15)–(18). These equations relate the interaction strengths at the two length scales and algebraic manipulation reveals the final forms $J'(J,K,\Delta)$, $K'(J,K,\Delta)$, and $\Delta'(J,K,\Delta)$ (see Sec. V for more details).

Repeated application of the recursion relations results in a renormalization-group trajectory that flows to a sink. From the nature of each trajectory and resulting sink, phase diagrams are mapped and transitions are characterized,

$$J' = R_J(J,K,\Delta), \qquad (8)$$

$$K' = R_K(J,K,\Delta). \qquad (9)$$

$$\Delta' = R_\Delta(J,K,\Delta). \qquad (10)$$

At each sink the values of the coupling coefficients (J,Δ) have reached fixed points, denoted by (J^*,Δ^*). Basins of attraction in parameter space, corresponding to bulk phases, flow to common fixed points (also known as sinks) (see Table I). The system is scale invariant in the vicinity of these fixed points and as a consequence the thermodynamic properties are unaffected by renormalization. Mathematically, the fixed points must satisfy the recursion relations such that

$$J^* = R_J(J^*,K^*,\Delta^*), \qquad (11)$$

$$K^* = R_K(J^*, K^*, \Delta^*), \qquad (12)$$

$$\Delta^* = R_\Delta(J^*, K^*, \Delta^*). \qquad (13)$$

Our basic generating unit for our hierarchical lattice consists of two types of components [see Figs. 2(a) and 2(b)] similar to Refs. [14,17–19,30]. Within each component, there exist two qualitatively different types of nearest-neighbor sites: those with interactions (J, Δ) and those with interactions $(J, -\Delta)$. The presence of two qualitatively unique nearest-neighbor interactions allows us to separate the hierarchical lattice into two sublattices, distinguished from one another by the type of interaction. Thus, each sublattice actually consists of the bonds rather than the sites themselves.

The degree of the competition between the two types of interactions is tuned by varying the strength of the crosslink interaction [Fig. 2(a)]. The special case of $p = 0$ yields the hierarchical model equivalent [28] to the Migdal-Kadanoff [31,32] decimation-bond moving scheme in two dimensions. For this study, the strength of the crosslink interaction (p), in Fig. 2(a), has been varied and the effects upon ordering have been presented for $p = 1, 2, 4,$ and 8. The end spins in the model are also allowed to interact via two connecting paths that do not have this crosslinked feature, as shown in Fig. 2(b). One type of path, consisting of m_1 pairs of spins, has all interactions of the same type, (J, Δ), while the other, with m_2 pairs of spins, has one nearest-neighbor pair that differs in the crystal-field interaction, $(J, -\Delta)$, from the rest of the connecting path. The motivation for including these different types of connecting paths stems from our desire to allow the end spins to interact via multiple paths, some with and some without competing interactions.

The connectivity of the system is varied using two parameters, p_A and p_B, each representing the number of component structures, of type A or type B, respectively, used in our basic unit generator for the hierarchical lattice as shown in Fig. 2(c). The present investigation has used connectivity parameters, $(p, m_1, m_2, p_A, p_B) = (4, 8, 9, 40, 1)$, that parallel those used in Refs. [14,17–19,30]. An increase in the level of connectivity beyond a critical threshold, before the effects of competing interactions are observed, is consistent with previous studies of spin-glass systems and other system [29] characterized by competing microscopic interactions.

III. PHASE TRANSITIONS

The phase diagrams produced in this investigation consist of multiple basins of attraction, each corresponding to a bulk phase each having its own sink to which repeated renormalization drives the coupling coefficients. Each phase is understood and interpreted by analyzing the nature of each respective sink. However, the nature of transitions between neighboring basins is also of interest to the present study. The order of each transition has been determined via careful calculation of thermodynamic properties for our system (e.g., magnetization, density, bilinear coupling, etc.) as phase boundaries are traversed in parameter space.

Each of these thermodynamic quantities is obtained via numerical differentiation of the free-energy density f—dimensionless Helmholtz (F) free energy per bond (N_b). The free-energy density consists of a sum of the contributions $G'^{(n)}$ to the free-energy density due to the internal degrees of freedom eliminated during each renormalization. The sum is over all applications of the renormalization-group transformation with each implementation reducing the length scale of the system by a factor of b and the number of spins by a factor of b^d,

$$f = -\frac{\beta F}{N_b} = \sum_{n=1}^{\infty} b^{-nd} G'^{(n)}(J^{(n-1)}, K^{(n-1)}, \Delta^{(n-1)}). \qquad (14)$$

Using the free-energy density, the magnetization, density, and bilinear correlations are calculated by measuring the shift in the free-energy density with a small perturbation in the magnetic field (i.e., $m \equiv \frac{M}{N_s} = \frac{N_b}{N_s} \frac{\delta f}{\delta H}$), crystal field (i.e., $\rho \equiv \frac{N_b}{N_s} \frac{\delta f}{\delta \Delta}$), and bilinear interaction (i.e., $\langle s_i s_j \rangle = s \frac{N_b}{N_s} \frac{\delta f}{\delta J}$), respectively, where N_s is the number of sites. First-order transitions will reveal themselves as discontinuities in any one of these thermodynamic quantities, whereas higher-order transitions will exhibit no such discontinuities but will yield critical scaling exponents as discussed in Sec. IV.

IV. RENORMALIZATION RELATIONS

By equating the fixed end spin configuration contributions, $R_l(s_i, s_j)$ and $R_{l'}(s_i, s_j)$, to the partition function from the two length scales (l and l'), we can write the following for the type A structure shown in Fig. 2(a):

$$
\begin{aligned}
R_l[1,1] &= \exp[-4\Delta] + 2\exp[-2J - \Delta(6-p) + 2K] + 2\exp[2J - \Delta(6-p) + 2K] + \exp[-\Delta(8-2p) + J(-4+p) \\
&\quad + K(4+p)] + 2\exp[-\Delta(8-2p) - Jp + K(4+p)] + \exp[-\Delta(8-2p) + J(4+p) + K(4+p)] \\
&= \exp[J' + K' - 2\Delta' + \widetilde{G}] = R_{l'}[1,1],
\end{aligned}
\qquad (15)
$$

$$
\begin{aligned}
R_l[1,0] &= \exp[-2\Delta] + 2\exp[-J - \Delta(4-p) + K] + 2\exp[J - \Delta(4-p) + K] + \exp[-\Delta(6-2p) + J(-2+p) + K(2+p)] \\
&\quad + 2\exp[-\Delta(6-2p) - Jp + K(2+p)] + \exp[-\Delta(6-2p) + J(2+p) + K(2+p)] \\
&= \exp[-\Delta' + \widetilde{G}] = R_{l'}[1,0],
\end{aligned}
\qquad (16)
$$

$$R_l[1,-1] = \exp[-4\Delta] + 4\exp[-\Delta(6-p)+2K] + 2\exp[-\Delta(8-2p)-Jp+K(4+p)] + 2\exp[-\Delta(8-2p)+Jp+K(4+p)]$$

$$= \exp[-J'+K'-2\Delta'+\tilde{G}] = R_{l'}[1,-1], \tag{17}$$

$$R_l[0,0] = 1 + 4\exp[-\Delta(2-p)] + 2\exp[-\Delta(4-2p)-Jp+Kp] + 2\exp[-\Delta(4-2p)+Jp+Kp] = \exp[\tilde{G}] = R_{l'}[0,0]. \tag{18}$$

Recursion relationships are derived, using the relationships above [Eqs. (15)–(18)], relating the strength of the coupling coefficients at the two different length scales (l and l') for the type A unit structure,

$$J'_A = \frac{1}{2} \ln \frac{R_{l'}(1,1)}{R_{l'}(1,-1)}, \tag{19}$$

$$K' = \frac{1}{2} \ln \frac{R_{l'}(1,1)R_{l'}(1,-1)R_{l'}^2(0,0)}{R_{l'}^4(1,0)}, \tag{20}$$

$$\Delta'_A = \ln \frac{R_{l'}(0,0)}{R_{l'}(1,0)}, \tag{21}$$

$$\tilde{G}'_A = \ln R_{l'}(0,0). \tag{22}$$

Recursion relations for type B unit structures involve a similar process and technique, including identical forms represented in Eqs. (19)–(22). However, the internal degrees of freedom removed with each renormalization differ. Therefore, the $R_l(s_i,s_j)$ contributions for the type B unit structure differ from the type A counterparts. Combining the contributions to the recursion relationships for both types of structures (type A and type B as shown in Fig. 2), the renormalization relationships become

$$J' = p_A J'_A + p_B J'_B, \tag{23}$$

$$K' = p_A K'_A + p_B K'_B, \tag{24}$$

$$\Delta' = p_A \Delta'_A + p_B \Delta'_B. \tag{25}$$

Exact relationships relating the coupling coefficients at length scales, l and l', allow for the precise calculation of critical scaling exponents. This is accomplished by linearizing the recursion relations in the vicinity of the critical transition under investigation. That is,

$$J' - J^* = T_{JJ}(J-J^*) + T_{JK}(K-K^*) + T_{J\Delta}(\Delta-\Delta^*), \tag{26}$$

$$K' - K^* = T_{KJ}(J-J^*) + T_{KK}(K-K^*) + T_{K\Delta}(\Delta-\Delta^*), \tag{27}$$

$$\Delta' - \Delta^* = T_{\Delta J}(J-J^*) + T_{\Delta K}(K-K^*) + T_{\Delta\Delta}(\Delta-\Delta^*), \tag{28}$$

where $T_{JJ} = \frac{\delta J'}{\delta J}$, $T_{\Delta J} = \frac{\delta \Delta'}{\delta J}$, etc. and are evaluated at the fixed point in question. The linearized recursion relationships can be represented as a recursion matrix, with elements T_{XY} and eigenvalues of the form

$$\Lambda_l = b^{y_l}, \tag{29}$$

where b is the length rescaling factor (in our case $b=2$) and y_l represents the corresponding critical exponent for the lth eigenvalue. A similar, independent analysis is also conducted for odd sector contributions, H and L.

V. RESULTS

Below we consider the effects of varying the temperature ($\sim 1/J$) and vacancy concentration ($\sim \Delta/J$) present in a system with competing crystal-field interactions. A series of phase diagrams are produced, each corresponding to a different level, via the tuning parameter p, of competing crystal-field interaction. In each plane, bulk phases have been mapped that are directly associated with basins of attraction arising from analysis of each renormalization-group trajectory. This investigation reveals four qualitatively unique regions (or basins of attraction), each sharing renormalization-group trajectories that flow to common sinks (see Table I).

Of the four unique basins of attraction, two structurally unique phases arise in parameter space: type I and type II. Type I phases (ferromagnet I and paramagnetic I) have a greater density of occupied sites on sublattice I, in comparison to a relatively dilute sublattice II. Type II phases, on the other hand, have a densely populated sublattice II and a sparsely populated sublattice I. Recall, the two sublattices are distinguished from one another by the type of couplings present, (J,Δ) for sublattice I and $(J,-\Delta)$ for sublattice II. Of the four phases identified, two are paramagnetic (paramagnetic I and paramagnetic II) with bilinear (J) renormalization trajectories flowing to zero indicative of no magnetic ordering. The flow of the crystal-field trajectory is the discriminating feature separating these two paramagnetic phases: paramagnetic I with the sink having ($\Delta \to -\infty$) and paramagnetic II with a flow for the crystal field ($\Delta \to +\infty$). For each paramagnetic phase there exists a ferromagnetic counterpart corresponding to a nonzero sink for the renormalization-group flow of the bilinear interaction ($J \to \infty$), indicating magnetic ordering.
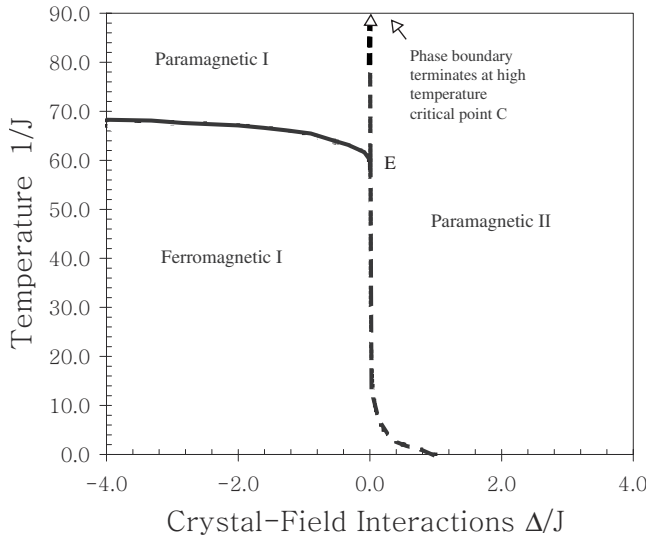
FIG. 3. Parameter space, temperature ($\sim 1/J$) versus vacancy concentration ($\sim \Delta/J$) with connectivity parameters $(p, m_1, m_2, p_A, p_B) = (1, 8, 9, 40, 1)$, depicting different basins of attraction and associated phases with critical end point (E) and critical point (C). Solid lines represent second-order transitions, whereas dashed lines represent first-order transitions.

When exploring parameter space with internal crosslink parameter $p = 1$ (Fig. 3) we find both paramagnetic phases, paramagnetic I and paramagnetic II, and the ferromagnetic I phase. The paramagnetic II phase dominates at all temperatures for larger values of the crystal-field interaction ($\sim \Delta/J$). At high temperatures, the paramagnetic II phase is separated from its paramagnetic I counterpart via a line of first-order transitions that terminates at a high-temperature critical point C, which is a critical point, above which it is possible to pass smoothly between the two phases as in the standard liquid-gas phase diagram. This line of first-order transitions separating the two paramagnetic phases has been probed, and latent heats observed, using the density on both sublattices (I and II) as the order parameter(s) for our system. This transition is analogous to liquid-liquid transitions observed in other systems. Sellitto [33] observed a similar first-order boundary separating two paramagnetic fluid phases in a study using mean-field models in conjunction with a Blume-Capel system to probe the phenomenon of inverse melting and freezing in structural glasses.

At lower temperatures, the paramagnetic II phase magnetically orders to the ferromagnetic I phase driven by a decreasing crystal-field interaction ($\sim \Delta/J$), corresponding to a smaller density of nonmagnetic impurities present. This same ferromagnetic I phase disorders to the paramagnetic I phase at high temperatures ($\sim 1/J = 70$) via a second-order phase transition. This line of second-order transitions terminating on the line of first-order transitions at a critical end point is similar to that topology observed by Hoston and Berker [9] for the case of uniform J, K, and Δ with $K/J = 5$, using mean-field theory.

As we increase the internal connectivity to $p = 2$ (Fig. 4) we see significant changes in the underlying phase diagram. The ferromagnetic I phase remains, as does its magnetically disordering transition, second order, at higher temperatures
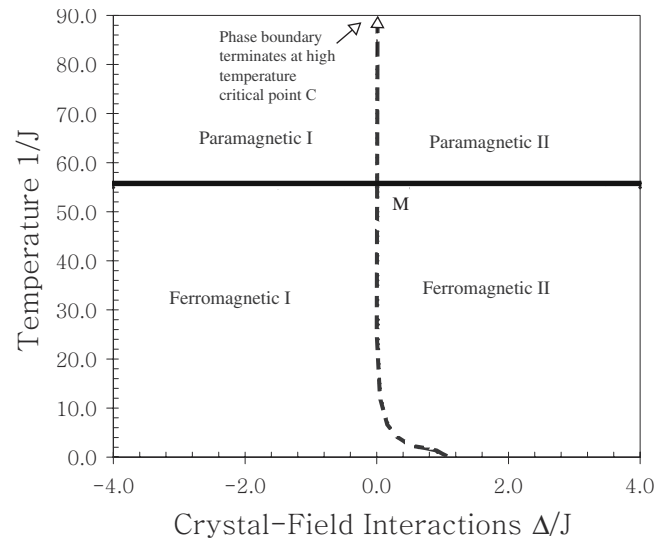
FIG. 4. Parameter space, temperature ($\sim 1/J$) versus vacancy concentration ($\sim \Delta/J$) with connectivity parameters $(p, m_1, m_2, p_A, p_B) = (2, 8, 9, 40, 1)$, depicting different basins of attraction and associated phases with multicritical point (M) and critical point (C). Solid lines represent second-order transitions, whereas dashed lines represent first-order transitions.

($1/J \sim 56$) to the paramagnetic I phase. However, a second disjoint ferromagnetic phase arises in parameter space, ferromagnetic II, for positive values of the crystal-field interaction. This ferromagnetic II phase also disorders via a line of second-order transitions at a temperature ($1/J \sim 56$) to its paramagnetic II counterpart. As the crystal-field interaction is varied from positive values to negative values the system undergoes a first-order transition from the ferromagnetic II phase to the ferromagnetic I phase. This crystal-field-driven transition corresponds to a redistribution of the nonmagnetic impurities present. Positive crystal-field interactions are conducive to ordering on sublattice II since the density of occupied sites is high, whereas, negative crystal-field interactions result in larger densities of occupied sites on sublattice I. Finally, the topology at the high-temperature crystal-field-driven first-order transition between the two paramagnetic phases persists for $p = 2$.

A further increase in the internal crosslink interactions to $p = 4$ (Fig. 5) reveals significant changes to the phase diagram, yet again. The ferromagnetic I phase is now present only at low temperatures. A low-temperature second-order transition separates the paramagnetic I and ferromagnetic I phases. In this model, the paramagnetic I phase orders to the ferromagnetic II phase via a first-order transition that is traversed as the crystal-field interaction increases from negative Δ/J to positive Δ/J. Lines of first-order transitions persist at low temperatures that separate the two ferromagnetic phases and terminates at the multicritical point P. Note that the high-temperature topology separating the two paramagnetic phases remains, as does the second-order transition from the ferromagnetic II to its paramagnetic II counterpart.

In our last phase diagram (Fig. 6), we explore the effects of varying temperature and crystal-field interactions upon ordering when increasing the magnitude of the internal
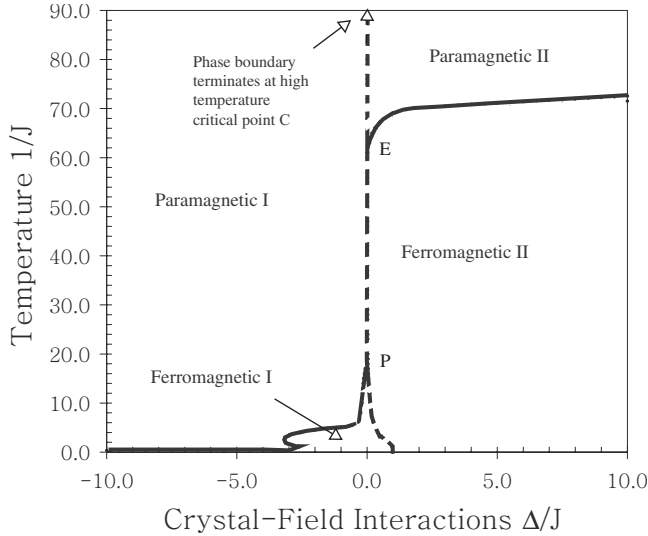
FIG. 5. Parameter space, temperature ($\sim 1/J$) versus vacancy concentration ($\sim \Delta/J$) with connectivity parameters $(p, m_1, m_2, p_A, p_B) = (4, 8, 9, 40, 1)$, depicting different basins of attraction and associated phases with critical end points (E and P) and critical point (C). Solid lines represent second-order transitions, whereas dashed lines represent first-order transitions.

crosslink interactions to $p=8$. Qualitatively, the phase diagram is very similar to the case of $p=4$. However, a noticeable difference is the size of the low-temperature ferromagnetic I region. An increase in internal connectivity parameter p drives this region to diminish in size.

In both of these last two phase diagrams, Figs. 5 and 6, corresponding to internal connectivities $p=4$ and $p=8$, there exists a small region, at low temperatures, in parameter space at which the system orders from the paramagnetic I phase to
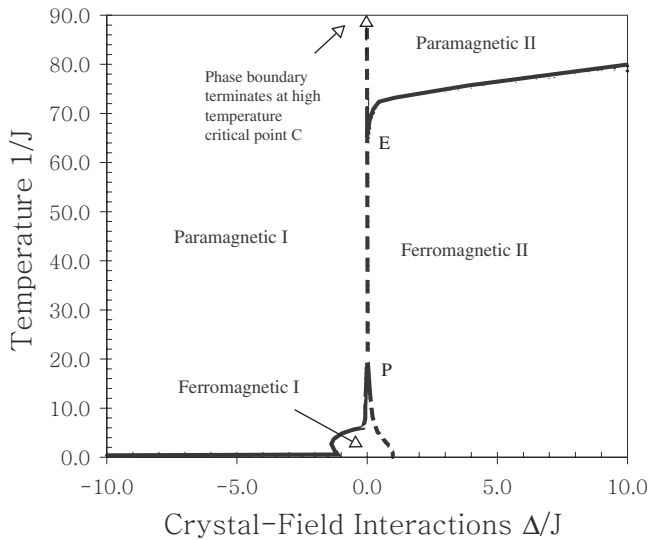
FIG. 6. Parameter space, temperature ($\sim 1/J$) versus vacancy concentration ($\sim \Delta/J$) with connectivity parameters $(p, m_1, m_2, p_A, p_B) = (8, 8, 9, 40, 1)$, depicting different basins of attraction and associated phases with critical end points (E and P) and critical point (C). Solid lines represent second-order transitions, whereas dashed lines represent first-order transitions.

its ferromagnetic I counterpart with an increase in temperature. This ordering transition, with an increase in temperature, seems to be in apparent contradiction to the expected increase in entropy. It appears that this may be an example of the phenomenon of inverse freezing. Physically our system consists of two sublattices (type I and type II). If ordering unexpectedly occurs (i.e., entropy decreases) with an increase in temperature on one sublattice (in this case sublattice I), then this must be compensated for by an increase in entropy on the other sublattice (in this case sublattice II). The free energy of the entire system consists of the contributions from both types of sublattices.

In each plane in parameter space considered in this study, lines of critical transitions have been probed while maintaining five scaling fields associated with J, K, Δ, H, and L. Linearization of the recursion relations, as discussed in Sec. IV, yields a recursion matrix from which eigenvalues and subsequent critical exponents are calculated. For the case of internal connectivity with $p=1$ the recursion matrix for the high-temperature paramagnetic I/ferromagnetic I second-order transition was found to have four relevant eigenvalues, $\Lambda_i = \{12.32, 5.00, 2.00, 2.00\}$, corresponding to critical scaling exponents of $y_i = \{3.62, 2.32, 1.00, 1.00\}$, respectively, and an irrelevant eigenvalue with $\Lambda_5 = -0.32$. In the $p=2$ case, both high-temperature second-order transitions, ferromagnetic I/paramagnetic I and ferromagnetic II/paramagnetic II transitions, yield four relevant eigenvalues with $\Lambda_i = \{13.40, 6.00, 2.00, 2.00\}$, corresponding to critical scaling exponents of $y_i = \{3.74, 2.58, 1.00, 1.00\}$, and an irrelevant eigenvalue with $\Lambda_5 = 0.60$

An increase in the strength of the internal connections with $p=4$ drives the critical line separating the ferromagnetic I and paramagnetic I phases to low temperatures. Analysis of the recursion matrix along this critical line yields three relevant eigenvalues, $\Lambda_i = \{9.15, 4.29, 1.48\}$, corresponding to critical scaling exponents of $y_i = \{3.19, 2.10, 0.566\}$, respectively, and two irrelevant eigenvalues with $\Lambda_4 = 0.755$ and $\Lambda_5 = 0.466$.

VI. SUMMARY

In summary, this investigation employs a hierarchical lattice and renormalization-group methodology to probe the effects of competing crystal-field interactions in a Blume-Capel Ising system. Several phase diagrams have been produced in temperature–crystal-field space as the strength of the competing crosslink crystal-field interactions is varied. Each sink has been interpreted and critical exponents have been calculated for the higher-order transitions.

This investigation found four different phases corresponding to four unique basins of attraction for the renormalization-group trajectories. Two paramagnetic phases (paramagnetic I and paramagnetic II) are separated at high temperatures by a first-order phase boundary that terminates at a high-temperature critical point C. This transition is not present in the original Blume-Capel model; however, a similar transition has been observed by Sellitto [33]. The ordering transitions from paramagnetic I (II) to ferromagnetic I (II) were found to be second order in each case they were

observed. The topography, presence, and location of these transitions are critically dependent on the internal connectivity parameter p. The phase boundary separating the paramagnetic I and ferromagnetic II phases, and also paramagnetic II and ferromagnetic I phases, was found to be first order in nature. In a small range in parameter space, a region of reentrance was found that corresponds to the system undergoing inverse freezing similar to that found in [8,33]. Thus, the hierarchical spin system presented here may provide another variation of the Blume-Capel model for further probing these

counterintuitive ordering transitions. In general, the results of this work offer additional insights into ordering in systems characterized by competing interactions that affect both the density and distribution of nonmagnetic impurities.

[1] M. Blume, Phys. Rev. **141**, 517 (1966).

[2] H. W. Capel, Physica **32**, 966 (1966).

[3] M. Blume, V. J. Emery, and R. B. Griffiths, Phys. Rev. A **4**, 1071 (1971).

[4] T. R. Kirkpatrick and D. Thirumalai, Phys. Rev. B **36**, 5388 (1987).

[5] A. Coniglio, J. Phys. IV **3**, C1–1 (1993).

[6] J. J. Arenzon, M. Nicodemi, and M. Sellitto, J. Phys. I **6**, 1143 (1996).

[7] M. Nicodemi and A. Coniglio, J. Phys. A **30**, L187 (1997).

[8] N. Schupper and N. M. Shnerb, Phys. Rev. E **72**, 046107 (2005).

[9] W. Hoston and A. N. Berker, Phys. Rev. Lett. **67**, 1027 (1991).

[10] M. Sellitto, M. Nicodemi, and J. J. Arenzon, J. Phys. I **7**, 945 (1997).

[11] D. P. Snowman, Ph.D. thesis, University of Maine, 1995.

[12] S. R. McKay and A. N. Berker, J. Appl. Phys. **55**, 1646 (1984).

[13] A. N. Berker and M. Wortis, Phys. Rev. B **14**, 4946 (1976).

[14] S. R. McKay, A. N. Berker, and S. Kirkpatrick, Phys. Rev. Lett. **48**, 767 (1982).

[15] N. S. Branco, Phys. Rev. B **60**, 1033 (1999).

[16] N. S. Branco and B. M. Boechat, Phys. Rev. B **56**, 11673

(1997).

[17] D. P. Snowman, J. Magn. Magn. Mater. **314**, 69 (2007).

[18] D. P. Snowman, J. Magn. Magn. Mater. **320**, 1622 (2008).

[19] D. P. Snowman, Phys. Rev. E **77**, 041112 (2008).

[20] A. Falicov and A. N. Berker, Phys. Rev. Lett. **76**, 4380 (1996).

[21] A. Kabakcioglu and A. N. Berker, Phys. Rev. Lett. **82**, 2572 (1999).

[22] N. S. Branco and L. Bachmann, Physica A **257**(1), 319 (1998).

[23] D. Andelman and A. N. Berker, Phys. Rev. B **29**, 2630 (1984).

[24] A. Falicov, A. N. Berker, and S. R. McKay, Phys. Rev. B **51**, 8266 (1995).

[25] G. Migliorini and A. N. Berker, Phys. Rev. B **57**, 426 (1998).

[26] R. A. da Silveira and J. P. Bouchaud, Phys. Rev. Lett. **93**, 015901 (2004).

[27] R. B. Stinchcombe and A. C. Maggs, J. Phys. A **19**, 1949 (1986).

[28] A. N. Berker and S. Ostlund, J. Phys. C **12**, 4961 (1979).

[29] M. Kaufman and R. B. Griffiths, Phys. Rev. B **24**, 496 (1981).

[30] S. R. McKay, A. N. Berker, and S. Kirkpatrick, J. Appl. Phys. **53**, 7974 (1982).

[31] A. A.Migdal, Zh. Eksp. Teor. Fiz. **69**, 1457 (1975).

[32] L. P. Kadanoff, Ann. Phys. (N.Y.) **100**, 359 (1976).

[33] M. Sellitto, Phys. Rev. B **73**, 180202(R) (2006).